

Origin of Negative Thermal Expansion and Pressure Induced Amorphization in Zirconium Tungstate from Machine- Learning Potential

Ri He¹, Hongyu Wu¹, Yi Lu^{2,3}, Zhicheng Zhong^{1,4*}

¹Key Laboratory of Magnetic Materials Devices & Zhejiang Province Key Laboratory of Magnetic Materials and Application Technology, Ningbo Institute of Materials Technology and Engineering, Chinese Academy of Sciences, Ningbo 315201, China

²National Laboratory of Solid State Microstructures and Department of Physics, Nanjing University, Nanjing 210093, China

³Collaborative Innovation Center of Advanced Microstructures, Nanjing University, Nanjing 210093, China

⁴China Center of Materials Science and Optoelectronics Engineering, University of Chinese Academy of Sciences, Beijing 100049, China

* zhong@nimte.ac.cn

Abstract

Understanding various macroscopic pressure-volume-temperature properties of materials on the atomistic level has always been an ambition for physicists and material scientists. Particularly, some materials such as zirconium tungstate (ZrW_2O_8), exhibit multiple exotic properties including negative thermal expansion (NTE) and pressure-induced amorphization (PIA). Here, using machine-learning based deep potential, we trace both of the phenomena in ZrW_2O_8 back to a common atomistic origin, where the nonbridging O atoms play a critical role. We demonstrate that the nonbridging O atoms confer great flexibility to vibration of polyhedrons, and kinetically drive volume shrinking on heating, or NTE. In addition, beyond a certain critical pressure, we find that the migration of nonbridging O atoms leads to additional bond formation that lowers the potential energy, suggesting that the PIA is a potential-driven first-order phase transition. Most importantly, we identify a second critical pressure beyond which the amorphous phase of ZrW_2O_8 undergoes a “hidden” phase transition from a reversible phase to an irreversible one.

Introduction

Macroscopic properties of materials are deeply rooted in their underlying atomic arrangement and interaction, and understanding these properties on an atomistic level has been a long-sought endeavor¹. Temperature and external pressure, two of the most commonly used “tuning knobs” for manipulating physical properties of materials to date, has led to the discovery of numerous exotic phenomena such as negative thermal expansion (NTE)^{2, 3, 4}, liquid-liquid second critical point^{5, 6, 7}, and pressure-induced high-temperature superconductivity^{8, 9, 10}. Establishing a clear relationship between these macroscopic properties and the atomistic behavior is not only important from a fundamental perspective, but also holds the key for rational material design. It yet remains a highly nontrivial task due to the large number of degrees of freedom inherent to a macroscopic system, which are usually difficult to be captured in microscopic theories.

Take the NTE for example, which refers to the counter-intuitive phenomenon that certain materials contract upon heating^{3, 4}. NTE materials are relatively rare and ZrW_2O_8 is the one of the most representative ones among them. ZrW_2O_8 exhibits volume reduction with increasing temperature from 0.3 K to 1050 K¹¹. The nature of the local mechanism responsible for its NTE remains controversial as the exact atomic structure details on heating can only be indirectly inferred from experiment with certain model assumption^{12, 13, 14}. One of the most common explanations is the Rigid Unit Modes (RUM) model, in which the transverse vibrations of O atoms can only occur through coupled liberations of tetrahedra and octahedra forming the structure^{15, 16, 17}, although its validity needs to be verified by microscopic calculations that has so far remained elusive.

In addition to NTE, ZrW_2O_8 exhibits another interesting property, namely the pressure-induced amorphization transition (PIA). Perottoni *et al.* showed that above 1.5 GPa, crystalline ZrW_2O_8 transforms to an amorphous phase that persists after pressure release at ambient conditions^{2, 18, 19}. While some theoretical research suggests that the PIA and NTE may have a common origin²⁰, the exact mechanism of PIA in ZrW_2O_8 are

still heavily debated^{21, 22, 23, 24, 25}, as the complexity of disordered atomic structure poses serious challenges to traditional theoretical methods such as the classical atomic force field, which describes bonded and nonbonded interactions in solids using some prescribed functions with fitted parameters that severely limit the flexibility of the force fields^{14, 15}. The lack of periodicity, and consequently a small enough unit cell, in amorphous materials also prevents its accurate description using methods such as density functional theory (DFT), whose computation complexity scales polynomially with the unit cell size.

To solve this outstanding problem and determine the atomistic origin of the NTE and PIA, in this study, we develop a machine learning (ML)-based deep potential (DP) for ZrW_2O_8 using training data from DFT calculations. ML-based potentials have the flexibility and non-linearity necessary to describe complex ordered and disordered interatomic environment from the perspective of “many-body” using a deep neural network^{26, 27}. While still in infancy state, they have been successfully applied to the investigation of various process in complex material systems²⁸, including phase transition^{29, 30, 31}, nucleation³², chemical catalysis³³, gas combustion³⁴, and atomic layer deposition of film growth³⁵. Herein, we find that the well-trained DP can describe the structure and other structure-related properties of ZrW_2O_8 over a wide temperature and pressure range. Using the DP, the calculated NTE and PIA in ZrW_2O_8 show great agreement with experimental results. Importantly, DP calculated results reveal that the NTE and PIA originate from a common factor, namely the nonbridging O atoms. For NTE, the nonbridging O confers great flexibility to the rotation of tetrahedra and octahedra that lead to volume contraction upon heating. In addition, the nonbridging O atoms move into a neighboring polyhedron above a critical pressure of 1.4 GPa and form additional bonds to lower the thermodynamical potential energy, driving a first-order amorphization phase transition as observed in experiments. Furthermore, we predict that further increasing the pressure to a second critical value of 3.8 GPa induces a “hidden” phase transition from an a^I reversible phase to an a^{II} irreversible one.

Results

Accurate Deep Learning Potential

The crystal structure of ZrW_2O_8 at 0 K to 430 K is cubic phase with $P2_13$ space group as illustrated in Fig. 1. The unit cell consists of a network of corner-shared octahedral ZrO_6 and tetrahedral WO_4 . The six octahedral ZrO_6 are equivalent and each share all their six corners with neighboring WO_4 tetrahedra, while the eight tetrahedral WO_4 each share only three of their four O atoms with the neighboring octahedral ZrO_6 , leaving one W-O bond dangling. We refer the corresponding O atom as the nonbridging O (marked by green spheres in Fig. 1). The tetrahedral WO_4 can be divided into two types depending on the length of nonbridging W-O bond. The WO_4 tetrahedrons with shorter (longer) W-O bond are labeled as $\text{W}^{\text{I}}\text{O}_4$ ($\text{W}^{\text{II}}\text{O}_4$). All the crystalline phase related results in the main text are based on the cubic α - ZrW_2O_8 , while the discussion of β -phase and γ -phase can be found in Supplementary Materials. The DFT optimized ground-state cubic phase is used as initial structure to explore all the characteristic configurations of high-temperature crystal and high-pressure amorphous. The 20460 configurations with different temperatures and pressures used in the training dataset are explored by the DP-GEN concurrent learning procedure³⁶, and the deep neural network-based DP is trained using the DeePMD method (for details, see Methods)^{26, 27}.

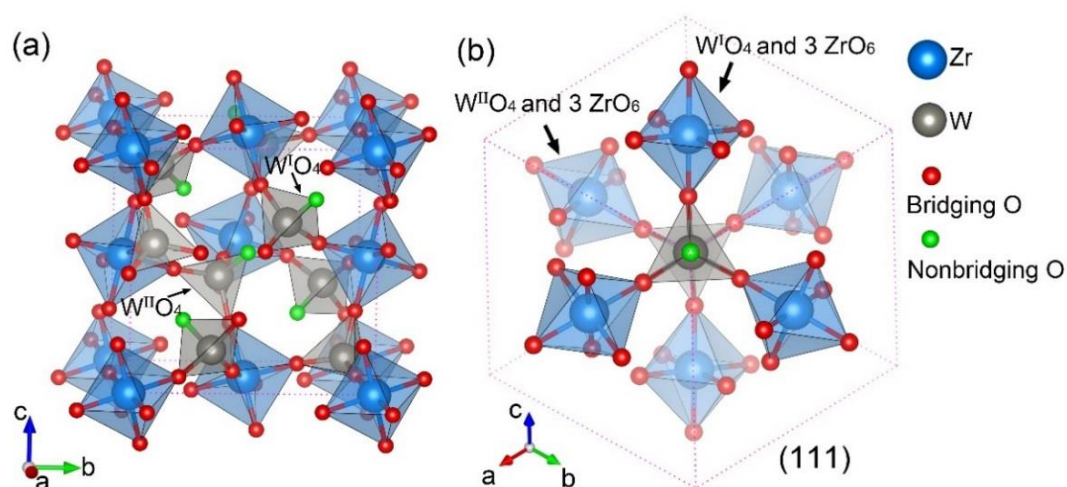


Fig.1 Structure of cubic ZrW_2O_8 unit cell. (a) The cubic cell consists of a network of corner-shared octahedral ZrO_6 and tetrahedral WO_4 . The octahedral ZrO_6 are equivalent but the

tetrahedral WO_4 can be divided into $\text{W}^{\text{I}}\text{O}_4$ and $\text{W}^{\text{II}}\text{O}_4$ depending on the length of nonbridging W-O bond. (b) $\langle 111 \rangle$ direction view of cubic cell.

Once the well-trained deep neural network-based DP is obtained, it is first benchmarked against DFT results to access its accuracy. We compare the energies and atomic forces calculated using the DP and DFT for 20460 configurations in the final training dataset. We find a good agreement between DP and DFT calculated energies and forces with a mean absolute error are 2.61 meV/atoms and 0.12 eV/Å, respectively, as shown in Fig. 2a, b. In comparison, the classical force field of ZrW_2O_8 proposed by Pryde et al.¹⁵ vastly overestimates atomic forces due to the limitations imposed by the preset functions and fitted parameters (see Fig. S1), and fails to predict atomic interactions involving the bond formation and breaking under pressure³⁷. The equations of state of cubic phase calculated by DFT and DP are presented in Fig. 2c. The DP model reproduces well the DFT energy profile over a wide range of lattice constants from 8.5 Å to 9.6 Å. The equilibrium lattice constants optimized by DFT and DP for cubic phase are 9.215 Å and 9.223 Å, respectively. We also use the DP to calculate the elastic constants for cubic phases and compare the values with DFT results. The results are shown in Table SI, again demonstrating great agreement between DP and DFT. Phonon dispersion spectrum is the quantum mechanical description of an atomic vibrational motion along different wave vectors, where the atomic force plays an important role. Accurate calculation of phonon dispersion is a strict criterion for testing the accuracy of DP. The calculated phonon dispersion of the cubic ZrW_2O_8 by the DP is shown in Fig. 2d. The 44-atom unit cell produces 3 acoustic and 129 optical branches. The 3 acoustic branches exist only in the low-frequency regime, and approach zero frequency towards the high-symmetry Gamma point. No negative phonon frequencies in the phonon dispersion indicates the dynamical stability of ZrW_2O_8 at room temperature and ambient pressure, which agrees well with the DFT results³⁸. The systematic benchmark shows that the DP has excellent DFT-level accuracy, and is capable of predicting a range of temperature and pressure properties of ZrW_2O_8 from first principles.

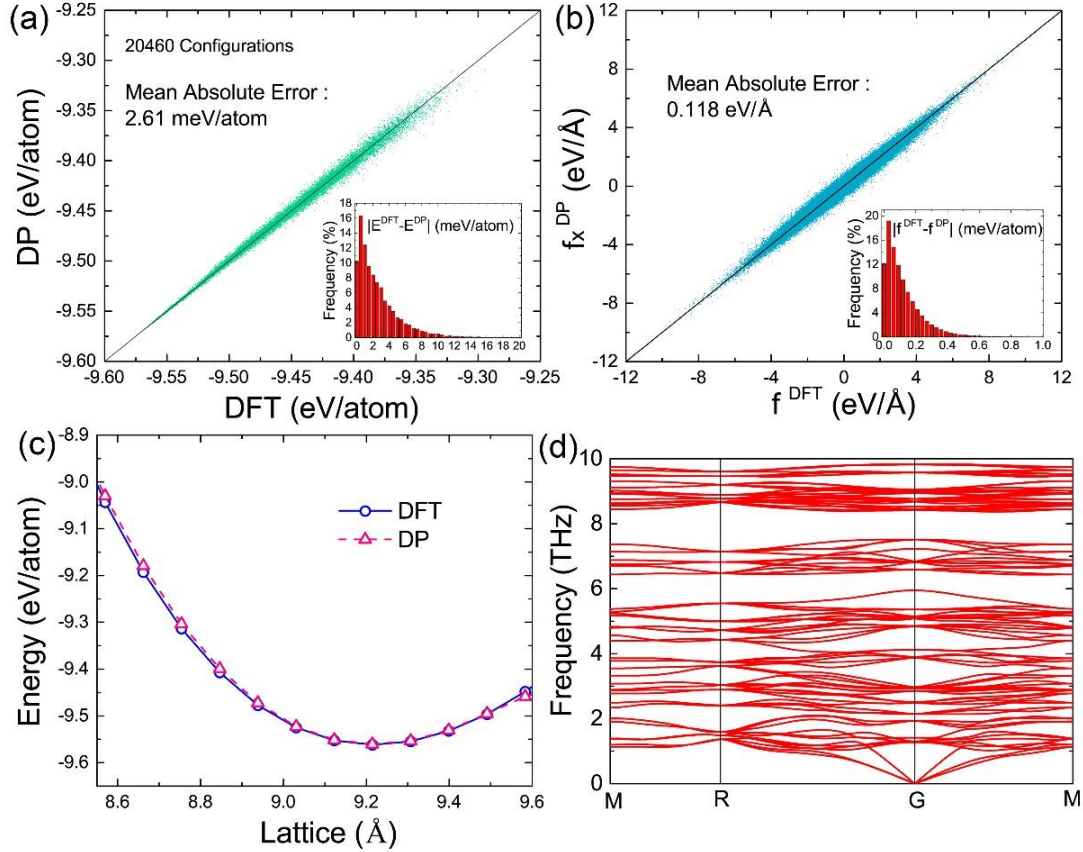


Fig. 2 The benchmark test of DP against DFT results. Comparison of energies (a) and atomic forces (b) calculated using the DP and DFT for all configurations. DP and DFT energies for different hydrostatic pressure (c) and phonon dispersion relations (d) for cubic phase.

The Origin of Negative Thermal Expansion

Once the DFT-level accuracy of DP is confirmed, we can use it to investigate the evolution of crystal structural properties of ZrW_2O_8 on heating by deep potential molecular dynamics (DPMD) simulations using a much larger system. Fig. 3a shows the lattice constant variation of a $7.3 \text{ nm} \times 7.3 \text{ nm} \times 7.3 \text{ nm}$ supercell (including 22528 atoms) with increasing temperature at ambient pressure. It can be clearly seen that the lattice constant exhibits a continuous shrink from 0 K to 1000 K (also see Supplementary Fig. S2). This result demonstrates an excellent isotropic NTE property of ZrW_2O_8 . The DP calculated coefficient of thermal expansion is $-6.2 \times 10^{-6} \text{ K}^{-1}$, in good agreement with reported experimental results of -4 to $-9 \times 10^{-6} \text{ K}^{-1}$.³⁹ The neutron pair distribution functions $G(r)$ at room temperature obtained with the DPMD

simulations is shown in Fig. 3b. The excellent agreement between the calculation and the experimental result²³ confirms that the DP can well capture the atomic structural characteristics of ZrW_2O_8 at room temperature.

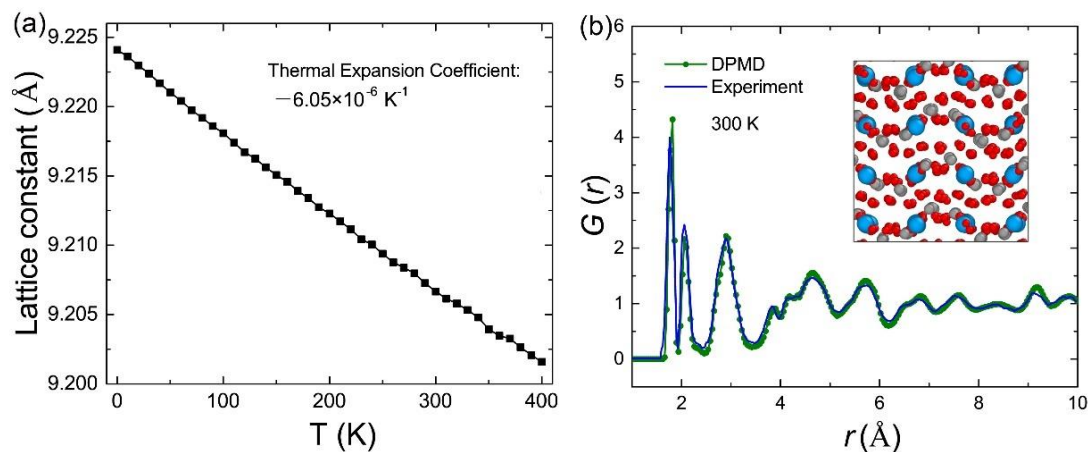


Fig. 3 Crystal structural properties of ZrW_2O_8 on heating. (a) Variation of cubic ZrW_2O_8 lattice parameter with temperature from DPMD at ambient pressure. (b) Neutron weighted pair distribution functions $G(r)$ from cubic ZrW_2O_8 at 300 K and 1 bar calculated from DPMD and experiment.

Despite the extensive study, the exact origin of NTE in ZrW_2O_8 is still controversial and has been attributed to a variety of mechanisms. For instance, the “RUM” model suggests that the transverse vibrations of the O atoms in the middle of W-O-Zr linkage are the result of whole-body rotations and translations of the linked octahedral ZrO_6 and tetrahedral WO_4 with essentially no distortion, pulling the Zr and W atoms closer and thus causing the NTE (a sketch is shown in Fig. S3)^{11, 15, 16, 17}. In contrast, the “Tent” model assumes a stiff W-O-Zr linkage, and NTE derives from the translational motion of tetrahedral WO_4 along the $\langle 111 \rangle$ direction and the correlated motion of the three nearest octahedral ZrO_6 ^{12, 13}. In other words, the main controversy between the RUM and Tent models lies in the relative stiffness of the W-O-Zr linkage.

To resolve the above controversy, we investigate the thermal expansion of neighboring atom pair distances (or bond length) and the degree of rigidity of corner-sharing polyhedrons. In DPMD simulations, each atom at \mathbf{r}_i vibrates about its mean position $\langle \mathbf{r}_i \rangle$. The atomic distances between two atoms can thus take an “apparent” value $\mathbf{R} = |\langle \mathbf{r}_i \rangle - \langle \mathbf{r}_j \rangle|$, which is the difference between their mean positions, and a

time-dependent “true” value $r = |\mathbf{r}_i - \mathbf{r}_j|$ ^{3, 14}. The former defines the lattice constants and can be directly determined by x-ray or neutron diffraction measurements. The latter contains more detailed dynamical properties of the lattice but is not easily probed in experiments. A similar consideration can be used to define “apparent” and “true” angles of W-O-Zr linkage. The DPMD results obtained for apparent and true bond length (atom pair distance) of W-O, Zr-O, Zr-W, Zr-Zr, and angle of Zr-O-W at different temperatures are presented in Fig. 4 (for W^IO₄ and three nearest ZrO₆) and Fig. S4 (for W^{II}O₄ and three nearest ZrO₆). It clearly indicates that the W-O (Zr-O) bonds display a negative thermal expansion coefficient of $-1.542 \times 10^{-5} \text{ K}^{-1}$ ($-0.377 \times 10^{-5} \text{ K}^{-1}$) for the apparent bond length, but a positive one of 0.504 K^{-1} ($1.548 \times 10^{-5} \text{ K}^{-1}$) for the true bond length. The DPMD results reveal that the asymmetry of atomic interaction potential causes an increase in the mean instantaneous distance between the bonded atoms as the temperature increases, but the distance between the mean positions of two atoms tend to decrease. These results show that both the RUM and Tent models are only partially right. On one hand, the observed expansion of the WO₄ tetrahedra and ZrO₆ octahedra invalidates the rigid-polyhedron assumption in RUM model. On the other hand, while the apparent W-O-Zr angle Φ remains nearly constant at ~ 155.5 degrees, in a seemingly agreement with the assumption of the Tent mode, the true W-O-Zr angle $\langle \phi \rangle$ decrease drastically with increasing temperature as shown in Fig. 4c. In reality, the expansion of true W-O and Zr-O bonds are overcompensated by the decrease of the true W-O-Zr angle caused by the transverse vibrations of the O atom in the middle of the Zr-O-W linkage (Fig. 4f), and their combined effect results in the observed NTE, as reflected in the reduction of the overall lattice constants as well as the Zr-W and Zr-Zr distances (Fig. 4d, e and Supplementary Fig. S5).

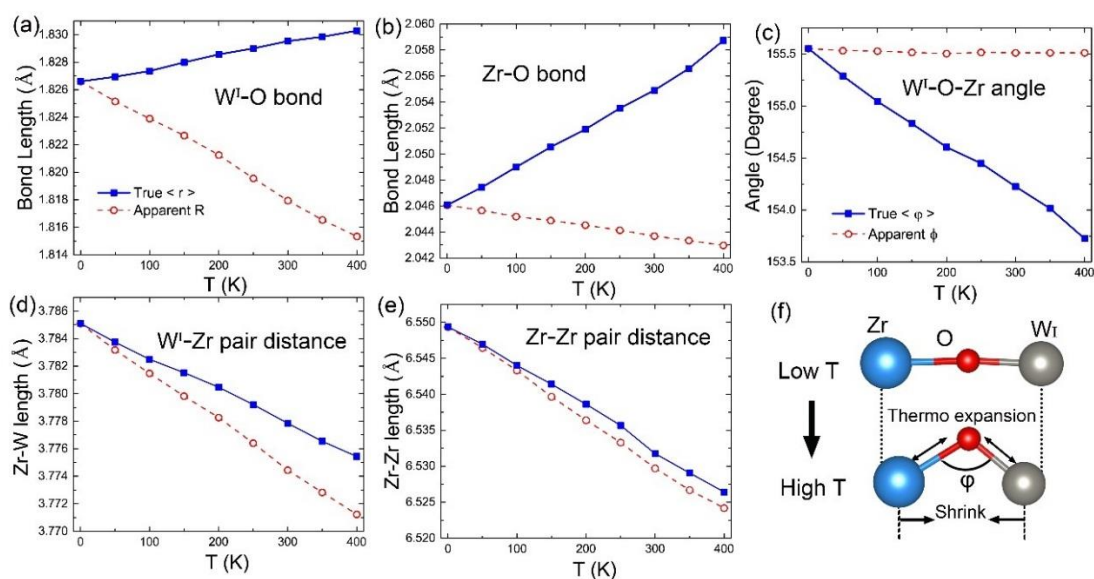


Fig. 4 Thermal expansion of neighboring atom pair distances and degree of corner-sharing polyhedrons. “True” and “apparent” bond length/atom pair of (a) W-O, (b) Zr-O, (d) Zr-W, (e) Zr-Zr, and angle of (c) Zr-O-W as a function of temperature. (f) The sketch of bond length and angle variation on heating.

Pressure Induced Amorphous Phase and its Reversibility

The amorphization transition under high pressure is another key feature of ZrW_2O_8 . While the NTE and the PIA are believed to be closely linked^{18, 23, 40}, the detailed complex atomic structure of amorphous ZrW_2O_8 has been a subject of debate. To resolve this issue, we further perform DPMD simulations of ZrW_2O_8 under different pressure (0.2 GPa ~ 4.4 GPa) at 300 K for 50 ps, with subsequent pressure relaxation to 1 bar for 100 ps. The structural properties as a function of time are shown in Fig. 5a, and the lattice constant dependence on pressure for compression (red line) and decompression (blue line) processes are shown in Fig. 5b. Upon application of pressure, it can be observed that the lattice constant decreases slightly by 0.05 Å from 1 bar to 1.3 GPa. Analysis of structural partial radial distribution functions (RDFs), obtained from DPMD simulations, can offer a detailed description of the observed structural phase transition from crystal to amorphous on an atomistic level. In the pressure range between 1 bar to 1.3 GPa, the partial O-O RDFs in Fig. 6a clearly show that the ZrW_2O_8 maintains perfect crystalline structure. The corresponding atomic structures of crystalline phase are shown in Supplementary Fig. S6 a-c. The crystalline ZrW_2O_8

under pressure still exhibits excellent NTE property (see Supplementary Fig. S7). Increasing the pressure beyond 1.4 GPa, the O-O RDF peaks vanish at distances larger than 8 Å (see Fig. 6a). This substantial modification indicates that ZrW_2O_8 undergoes an amorphization transition. The snapshots of corresponding atomic structures for 1 bar to 2.5 GPa in Supplementary Fig. S6 also clearly show that a disordered structure form above 1.4 GPa. Accompanying the PIA is a sudden decrease of lattice constant from 9.16 to 8.89 Å (Fig. 6b), which shows the first-order nature of the phase transition. The amorphous ZrW_2O_8 does not exhibit NTE properties as shown in Supplementary Fig. S7. The calculated PIA critical pressure 1.4 GPa is well comparable to the experimental value of 1.5 GPa².

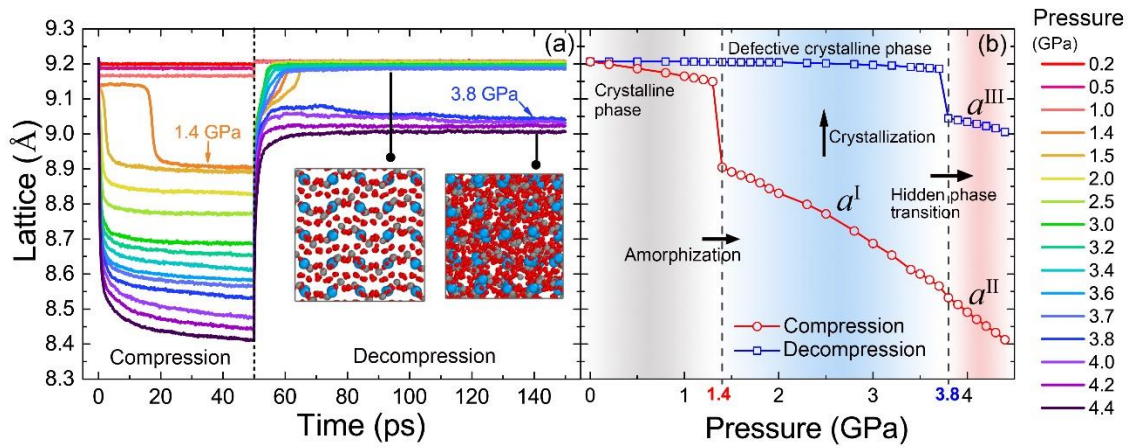


Fig. 5 **Structural properties of ZrW_2O_8 with compression and decompression.** (a) Variation of lattice parameter with time on compression from 0.2 GPa to 4.4 GPa at 300 K and then upon decompression. (b) The lattice parameter depends on pressure for compression after 50 ps (red line) and decompression after 100 ps (blue line).

To reveal the exact origin of PIA in ZrW_2O_8 , we explore the energy stability of cubic and amorphous phases as a function of hydrostatic pressure (i.e. lattice isotropic variation) by DP atomic relaxation at absolute zero, which will eliminate the contribution of kinetic energy induced by thermal perturbation. We emphasize that such calculations for amorphous phase are far beyond the capacity of DFT because of calculating spatial scale limitation. In the calculations, the amorphous phase can be stabilized strain-free with the optimized lattice constant 9.005 Å, much smaller than the 9.224 Å for cubic phase, and the corresponding atomic structures are shown in

Supplementary Fig. S8a, b. The resulting energy-versus-lattice diagram is shown in Fig. 6b. It shows that the amorphous phase is energetically favored for lattice constant smaller than ~ 9.13 Å. As lattice constant is increased, the amorphous phase rapidly becomes unstable and transitions to a “defective” crystalline structure, where a small number of O atoms could not return to its perfect lattice site, forming edge-shared polyhedral defects in cubic phases as shown in Fig. Supplementary S8c (it will be explained in detail below). The energy of these defective cubic phases is very close to that of perfect cubic phase, as shown by green triangles in Fig. 6b. Our results show that the driving force of PIA in ZrW_2O_8 is the potential energy.

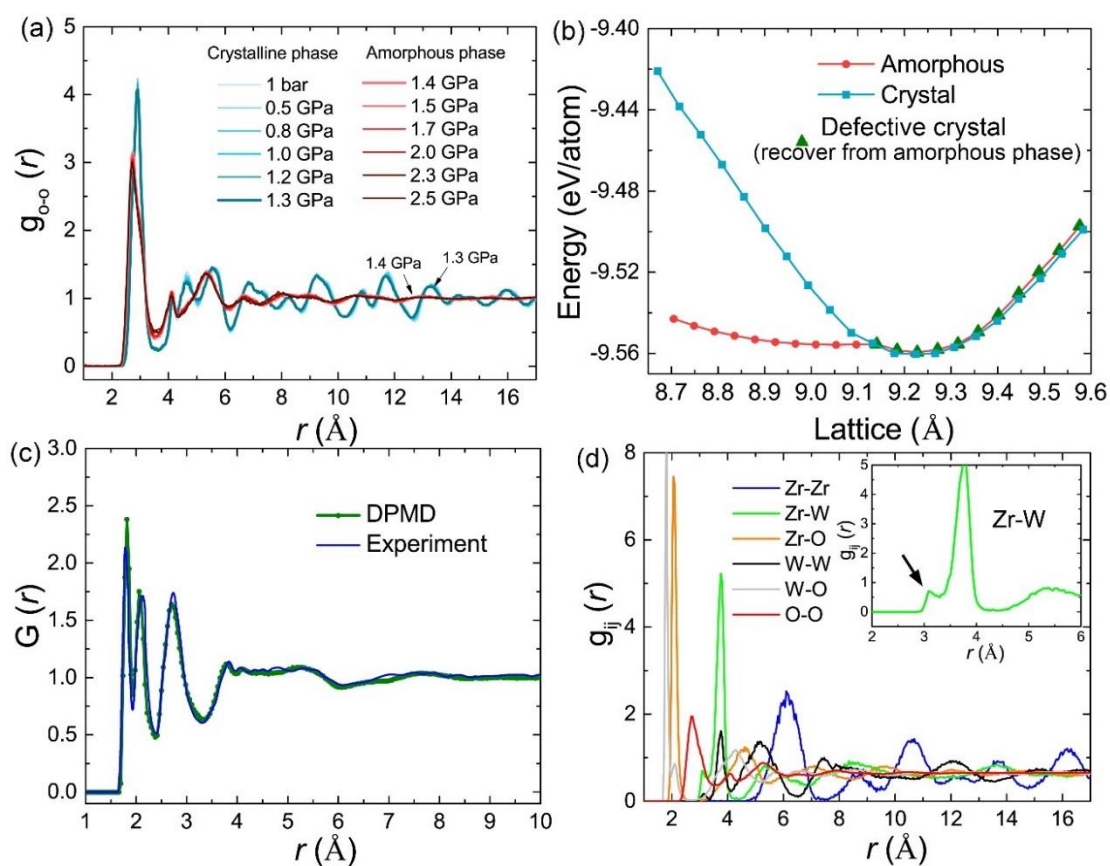


Fig. 6 Analysis of the atomic structure and potential energy of ZrW_2O_8 at different pressures. (a) Partial O-O RDFs, $g_{\text{O-O}}(r)$, of ZrW_2O_8 at different pressures from DPMD simulations at 300 K. (b) Energy variations of cubic and amorphous phase ZrW_2O_8 with hydrostatic pressure (lattice parameter variation), and amorphous is energy favored for the lattice constant is smaller than ~ 9.13 Å. (c) Neutron weighted pair distribution functions $G(r)$ and (d) radial distribution function $g_{ij}(r)$ of amorphous ZrW_2O_8 at 3 GPa calculated from DP model and experiment.

We proceed to analyze the detailed local structure of the amorphous phase. The DP calculated neutron weighted pair distribution functions $G(r)$ and partial RDF $g_{ij}(r)$ of

the amorphous phase at 300 K and at 3 GPa are shown in Fig. 6c, d. The calculated $G(r)$ is almost on top of the experimental data²³. We analyze the dynamic behavior of atoms during the amorphization transition under pressure. The local dynamic processes are shown in Fig. 7a-c. As mentioned above, ZrW_2O_8 crystallizes in cubic phase with the networks of corner-linked octahedral ZrO_6 and tetrahedral WO_4 , which is highly flexible. As the high pressure (above 1.4 GPa) is applied, the one nonbridging O in $\text{W}^{\text{I}}\text{O}_4$ (green spheres in Fig. 7a) moves into a neighboring octahedral ZrO_6 , and another one in $\text{W}^{\text{II}}\text{O}_4$ moves to a neighboring tetrahedral $\text{W}^{\text{I}}\text{O}_4$ (Fig. 7b), forming an edge-shared decahedral ZrO_7 and pentahedral $\text{W}^{\text{I}}\text{O}_6$ structure as shown in Fig. 7c. This edge-shared structure produces the first peak in 3.14 Å of partial RDF of Zr-W (marked by arrows in inset of Fig. 6d). The weakness of that peak intensity indicates that the above dynamic behavior happens randomly throughout the system. The equilibrated snapshot of the supercell after amorphization at 3 GPa is shown in Supplementary Fig. S9, several unique configurations of corner-shared and edge-shared polyhedron were formed by movement of nonbridging O atoms. Examination of the species-specific structure in Fig. 7d (with the corresponding RDFs in Fig. 6d) reveals an interesting aspect of the amorphous phase: the amorphous-like O sit within an almost periodic crystal-like Zr and W coordination array. We note that this structure is in consistent with the proposed Reverse Monte Carlo model of amorphous ZrW_2O_8 fitting from experiment data²³.

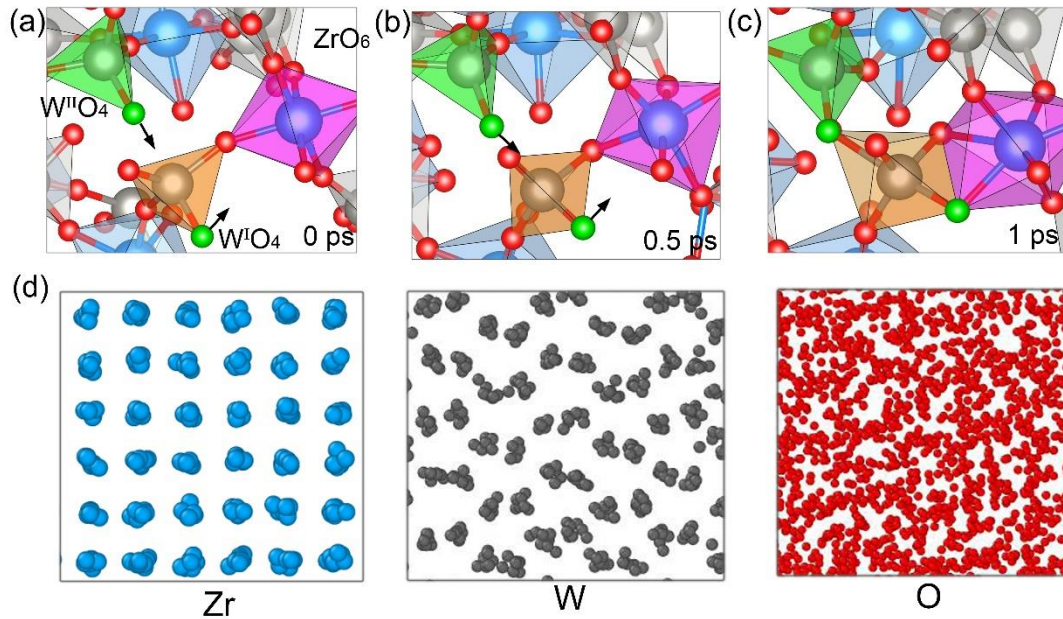


Fig. 7 Atomic structure evolution of amorphous ZrW_2O_8 at 3 GPa. (a)-(c) the movement of nonbridging O (marked in green) result in formation of ZrO_7 decanedron and WO_5 octahedron. (d) A part snapshot of amorphous 22528-atom supercell, the arrangements of Zr, W, and O are presented respectively.

We next consider the reversibility of the amorphous phase upon decompression. Experiments have confirmed that the PIA in ZrW_2O_8 is irreversible at room temperature, and recrystallization only occurs when heated above 900 K^{2, 40}. In this study, the subsequent DPMD simulations were performed for decompressions from various pressures (0.2 GPa ~ 4.4 GPa) to ambient conditions. The decompression structural property and RDFs results are shown in Fig. 5 (the atomic structures are shown in Supplementary Fig. S10) and Fig. 8 (also see Supplementary Fig. S11), and it indicates that pressure-induced amorphous phase can be divided into two categories. (i) For the amorphous phase with 1.4 GPa to 3.7 GPa, significant modifications in the RDF of W-W are observed upon decompression. The second peak at 4.1 Å becomes weaker while a new peak at slightly longer distance, 4.4 Å, appears, which indicates it can recover to crystalline phase after pressure release, so that we defined it as the a^I reversible phase. (ii) For the amorphous with pressure above 3.8 GPa, the RDFs results show that the amorphous phase can be retained upon decompression, which we defined as the a^{II} reversible phase. The same profiles of RDFs of a^I and a^{II} phases in Fig. 8a and

Supplementary Fig. S11a indicate that they have the same equilibrated atomic structure, and they cannot be distinguished by structural characterization in experiment. Therefore, we suggest that amorphous phase undergoes a “hidden” phase transition from a^I to a^{II} amorphous phase at the second critical pressure of 3.8 GPa. The RDF of retained a^{III} amorphous is slightly different from the a^I and a^{II} phase, but it exhibits the almost key features of amorphous phase (Fig. 8b and Supplementary Fig. S11b). The retained a^{III} amorphous phase is quite stable, because it was maintained in subsequent annealing for a long time of 2 ns, as well as at higher temperature of 400 K (Supplementary Fig. S12). It should be emphasized that the critical pressure of “hidden” phase transition slightly depends on compression time. For instance, the compression time increase from 50 ps to 300 ps, the critical pressure decreases from 3.8 GPa to 3.5 GPa (Supplementary Fig. S13).

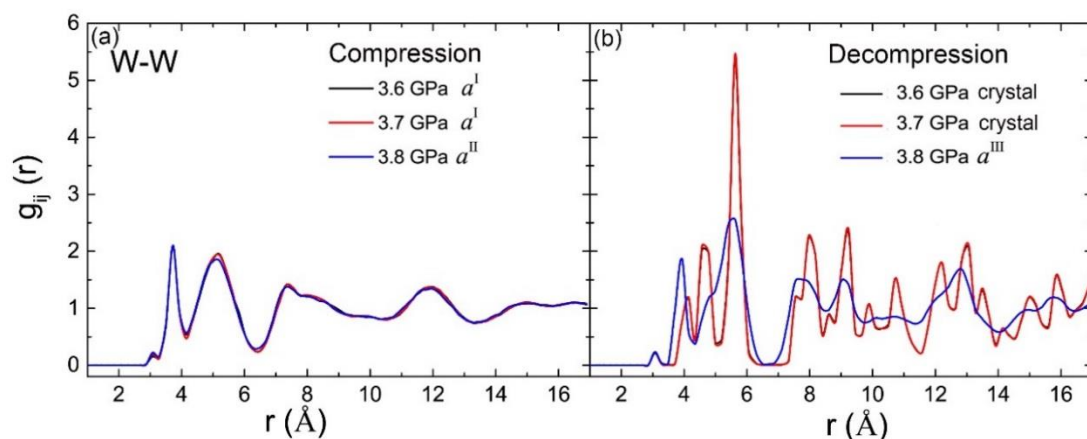


Fig. 8 Partial W-W RDFs of ZrW_2O_8 at different pressures. (a) RDFs at different pressure, (b) RDFs upon decompression.

For the defective crystalline phase that recovered from a^I phase, the partial W-W RDF is consistent with most of the characteristics of perfect crystalline phase by comparing Supplementary Fig. S11b and Fig. S14, except for an additional $g(r)_{w-w}$ peak in the ~ 3.16 Å (marked by arrows in Fig. 9a). The first additional of $g(r)_{w-w}$ originates from the edge-shared WO_5/WO_6 polyhedrons structures in crystalline phase upon decompression. This edge-shared structure can be regarded as a defect in the crystal, that formed when compression. By comparing the sliced atomic structure of a^I amorphous phase (3.7 GPa) and recovered crystalline phase in Fig. 9c, we found that

edge-shared WO_5/WO_6 polyhedrons are irreversible during crystallization, which is accord with the RDF result in Fig. 9a. On the contrary, the Fig 9b shows the first peak of $g(r)_{\text{Zr-W}}$ disappears in the recovered crystalline phase, which indicates the edge-shared decahedral ZrO_7 and octahedral WO_5 structure recovers to original octahedral ZrO_6 and tetrahedral WO_4 upon decompression (atomic structure evolution is shown in Fig. 9d). The entire sliced atomic structures are shown in Supplementary Fig. S15. To sum up, the edge-shared WO_5/WO_6 polyhedrons are stable and hard to be destroyed, whereas the edge-shared ZrO_7 and WO_5 polyhedrons are relatively unstable.

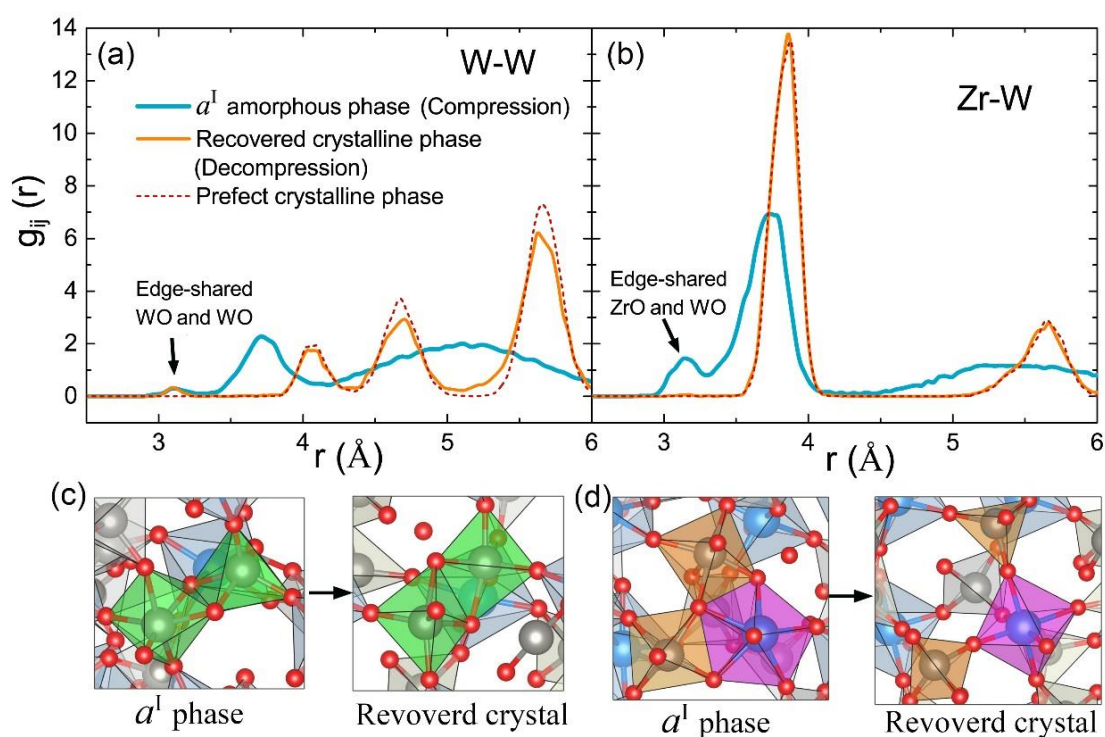


Fig. 9 Analysis of the atomic structure upon decompression. The partial RDFs $g(r)_{ij}$ of pressure-induced a^I amorphous (3.7 GPa) and recovered crystalline phase upon decompression for (a) W-W and (b) Zr-W. The first peak of $g(r)_{\text{W-W}}$ and $g(r)_{\text{Zr-W}}$ marked in figure corresponding to the edge-shared WO_4/WO_5 and $\text{ZrO}_7\text{-WO}_6$ polyhedrons. The atomic structural evolution of (c) edge-shared WO_4/WO_5 and (d) $\text{ZrO}_7\text{-WO}_6$ polyhedrons from a^I phase to recovered crystalline phase.

Conclusions

We have demonstrated that ML-based DP can reach an unprecedented level of accuracy in the atomic structural modeling of NTE and PIA materials over a wide

temperature and pressure range using the example of ZrW_2O_8 . The DP calculated NTE behavior and coefficient of thermal expansion in ZrW_2O_8 show great agreement with experimental results. By lattice dynamics study of local lattice vibrations, we have shown that both the current RUM and Tent models are only partially reasonable, and the NTE in ZrW_2O_8 originate from the large transverse vibrations of the O atoms in the middle of the Zr-O-W linkage. We further investigated the mechanism of PIA in ZrW_2O_8 . We found that ZrW_2O_8 undergoes a first-order potential-driven amorphization transition above a critical pressure of 1.4 GPa, which is well comparable to experimental value. We also reveal that the migration of O atoms leads to additional bond formation that lowers the potential energy, suggesting that the PIA is a potential-driven transition. Most importantly, we predicted that the amorphous phase undergoes a “hidden” phase transition from reversible a^I to irreversible a^{II} phase at a second critical pressure of 3.8 GPa, which shall be verified in future experiments. Our study on ZrW_2O_8 not only have important implications for future research on other NTE and PIA materials, but also opens the door for quantitatively accurate atomistic modeling of general materials with direct links to experiments. We believe that the DP method will play a pivotal role in future design of structural and functional materials whose properties depend sensitively on detailed atomic configurations.

Methods

1. Concurrent learning procedure

Carefully choose the ZrW_2O_8 configurations that used in the training dataset is crucial to the success of training process and accurate of DP. Because we focus on the NTE and PIA behaviors of ZrW_2O_8 , we need all the characteristic configurations of crystal and amorphous at a wide temperature and pressure range. Most of configurations that we need are far from the ground state of cubic phase. In this work, we use the DP Generator (DP-Gen) to generate a set of training data that covers an enough wide range of relevant configurational space efficiently. DP-Gen is a concurrent learning strategy³⁶,

and the workflow of each iteration includes three main steps as illustrated in Fig. 10: (1) Training the deep learning potentials, (2) exploration configurations by DPMD simulations, (3) labeling configurations according to certain criterion and added into training dataset.

We start with DFT optimized ground-state structures of $P2_13$ cubic phase ZrW_2O_8 . The DFT calculated lattice constant with Perdew-Burke-Ernzerhof solid (PBEsol) is 9.215 Å, slightly larger than 9.160 Å in experiment¹¹. In first iteration of DP-Gen workflow, the configurations of initial training dataset contain 200 randomly perturbed structures of 44-atoms cubic cell. The maximum magnitude of perturbed displacement for atomic coordinates is 0.01 Å, and the strain is -0.003 to 0.003 of the ground-state lattice parameters. Starting with above training datasets, four different DPs are trained using DeepMD method^{26, 27}, based on different values of deep neural network parameters. The exploration step was performed in which one of the DPs is used for MD simulations at given pressure and temperature to explore the configuration space. For all sampled configurations in MD trajectories, the other three DPs will predict the atomic forces of all atoms. The maximum deviation of the four DPs predicted forces (σ_f^{\max}) can be used to formulate the criterion for labeling configurations:

$$\sigma_f^{\max} = \max \sqrt{\langle |F_i - \langle F_i \rangle|^2 \rangle},$$

Where $\langle \dots \rangle$ indicates the average of DP predicted force, and F_i denotes the predicted force on the atom i . The explored configurations possess the characteristic of $\sigma_f^{\max} < \sigma_{low}$ indicates they are already well described with a high accuracy by the current DP, which are labeled as accuracy, whereas a explored configuration with $\sigma_f^{\max} > \sigma_{high}$ is highly distorted and unphysical due to poor model quality of DP and is thus labeled as failure. The failure ratio is often high in the first several iterations. Only configurations satisfying $\sigma_{low} < \sigma_f^{\max} < \sigma_{high}$ are selected as candidates for further self-consistent DFT calculation and are added to the training dataset for training in the next iteration. The σ_f^{\max} can be also used as the convergence criterion for DP-Gen iterations, and the DP-Gen iterations are considered converged when the accuracy ratio

is large than 99 %. Here, the σ_{low} and σ_{high} are set to 0.05 and 0.15 eV/Å in the iterations for 50 K to 550 K, and 0.08 and 0.25 eV/Å in the iterations for 600 K to 1500 K to ensure the convergence. Finally, by iterating above procedure 56 times, 20460 configurations were obtained for training. For more details of the DP-Gen process, please refer to the original literature or our previous work of developing SrTiO₃ DP³¹.

36.

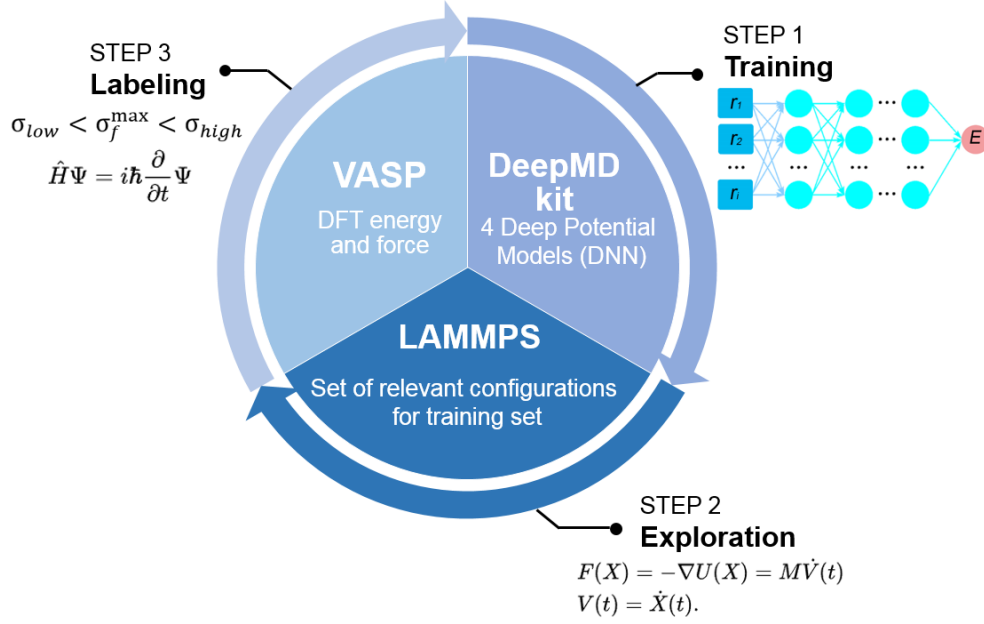


Fig. 10 The deep learning potential training procedure, including training, exploration, and labeling.

2. Training the DP

The DeePMD-kit code is used for training of DP⁴¹. In the deep neural network of DP, the total potential energy of a configuration is assumed to be a sum of each atomic energy, which is mapped from a descriptor through an embedding network. The descriptor characterizes the local environment of atom within a cutoff radius R_c . Here, the R_c is set to 6 Å. The maximum number of atoms within the R_c is set to 50 for Zr, 100 for W, and 400 for O, respectively. The translational, rotational, and permutational symmetry of the descriptor are preserved by another embedding network. The smooth edition of the DP model was employed to remove the discontinuity introduced by the R_c ²⁷. The sizes of the embedding and fitting networks are (25, 50, 100) and (240, 240, 240), respectively. The loss function that used in this work have the same form as our

recent work³¹. The weight coefficients of the energy, atomic force and virial terms in the loss functions change during the optimization process from 0.2 to 1, 500 to 1, and 0.02 to 0.2. The DPs are trained with 1 800 000 steps by learning rate decaying from $1e-3$ to $3.5e-8$ exponentially. The model compression scheme was applied in this work for boosting the computational efficiency of the DPMD simulation⁴².

3. DFT calculations

The initial training dataset in the first iteration is obtained by performing a 10-step *ab initio* MD simulation for randomly perturbed 44 atoms cubic cell at 50 K. After labeling candidate configurations, self-consistent DFT calculations were performed subsequently. The DFT calculations were performed using a plane-wave basis set with a cutoff energy of 500 eV as implemented in the Vienna Ab initio Simulation Package^{43, 44}, and the electron exchange-correlation potential was described using the generalized gradient approximation and PBEsol scheme⁴⁵. The Brillouin zone was sampled with a $4 \times 4 \times 4$ Monkhorst-Pack k-point grid for the cubic unit cell.

4. Molecular dynamics simulations

In exploration step, the MD simulations were performed using LAMMPS code with periodic boundary conditions⁴⁶. The MD simulations adopt the isobaric-isothermal (NPT) ensemble with temperature set from 10 to 1500 K and pressure set from 1 bar to 5 GPa, because the explorative temperature and pressure should be large than the ones for subsequent NTE and PIA simulations. A Nose-Hoover thermostat and Parrinello-Rahman barostat are employed to control temperature and pressure, respectively^{47, 48}. The time step in simulations is set to 1 fs.

The optimized DP can be used to study the atomic dynamics driven by temperature and pressure via performing deep potential MD (DPMD) simulations. The DPMD simulations starting with $8 \times 8 \times 8$ supercell (i.e. $7.3 \text{ nm} \times 7.3 \text{ nm} \times 7.3 \text{ nm}$) of optimized cubic $\alpha\text{-ZrW}_2\text{O}_8$ phase containing 22528 atoms. All results about NTE and PIA of ZrW_2O_8 were executed by DPMD simulations. For NTE simulations, the equilibrium run is 50 ps, followed by a production run of 100 ps at a specified temperature. The lattice constant, true/apparent bond length (angle) were calculated by the average of

200 snapshots in 100ps of equilibrium state. For PIA simulations, cubic symmetry was imposed (isotropic changes in cell lengths) during NPT simulations. The “lattice constants” of pressure-induced amorphous phase is defined as $\sqrt[3]{V}/8$, where V is the volume of the simulated $8 \times 8 \times 8$ supercell. The simulation time for compression and decompression were set to 50 ps and 100 ps, respectively. To prove the stability of retained a^{III} amorphous phase, we lengthen the decompression time to 2 ns, and found the a^{III} amorphous phase is maintained (Supplementary Fig. S11). We also lengthen the compression time to prove the second critical pressure of 3.8 GPa slightly depends on compression time (Supplementary Fig. S12).

Data availability

All the input files, final training datasets, and DP model files to reproduce the results contained in this paper are available in DP-library website <https://dplibrary.deepmd.net/>⁴⁹.

Code availability

The DFT calculations, MD simulations, concurrent learning procedure, and deep neural network training were performed with VAPS, LAMMPS, DP-GEN, and DeePMD-kit code. The latter three are open source codes available at <https://lammps.sandia.gov> and <https://github.com/deepmodeling>.

Acknowledgements

This paper was supported by the National Key R&D Program of China (Grants No. 2021YFA0718900, and No. 2017YFA0303602), the Key Research Program of Frontier Sciences of CAS (Grant No. ZDBS-LY-SLH008), the National Nature Science Foundation of China (Grants No. 11974365), the K.C. Wong Education Foundation (GJTD-2020-11).

Additional information

Supplementary information is available for this paper at <https://doi.org/XXXX>

References

1. Dove MT. *Structure and dynamics: an atomic view of materials*. Oxford University Press (2003).
2. Perottoni CA, Jornada JAHd. Pressure-Induced Amorphization and Negative Thermal Expansion in ZrW_2O_8 . *Science* **280**, 886-889 (1998).
3. Barrera GD, Bruno JAO, Barron THK, Allan NL. Negative thermal expansion. *J Phys-Condens Matter* **17**, R217-R252 (2005).
4. Miller W, Smith C, Mackenzie D, Evans K. Negative thermal expansion: a review. *Journal of materials science* **44**, 5441-5451 (2009).
5. Poole PH, Sciortino F, Essmann U, Stanley HE. Phase behaviour of metastable water. *Nature* **360**, 324-328 (1992).
6. Mishima O, Stanley HE. Decompression-induced melting of ice IV and the liquid-liquid transition in water. *Nature* **392**, 164-168 (1998).
7. Woutersen S, Ensing B, Hilbers M, Zhao Z, Angell CA. A liquid-liquid transition in supercooled aqueous solution related to the HDA-LDA transition. *Science* **359**, 1127-1131 (2018).
8. Drozdov AP, Erements MI, Troyan IA, Ksenofontov V, Shylin SI. Conventional superconductivity at 203 kelvin at high pressures in the sulfur hydride system. *Nature* **525**, 73-76 (2015).
9. Drozdov AP, *et al.* Superconductivity at 250 K in lanthanum hydride under high pressures. *Nature* **569**, 528-531 (2019).
10. Snider E, *et al.* Room-temperature superconductivity in a carbonaceous sulfur hydride. *Nature* **586**, 373-377 (2020).
11. Mary TA, Evans JSO, Vogt T, Sleight AW. Negative Thermal Expansion from 0.3 to 1050 Kelvin in ZrW_2O_8 . *Science* **272**, 90-92 (1996).
12. Cao D, Bridges F, Kowach GR, Ramirez AP. Frustrated Soft Modes and Negative Thermal Expansion in ZrW_2O_8 . *Phys Rev Lett* **89**, 215902 (2002).
13. Cao D, Bridges F, Kowach GR, Ramirez AP. Correlated atomic motions in the negative thermal expansion material ZrW_2O_8 : A local structure study. *Phys Rev B* **68**, 014303 (2003).
14. Sanson A. Toward an Understanding of the Local Origin of Negative Thermal Expansion in ZrW_2O_8 : Limits and Inconsistencies of the Tent and Rigid Unit Mode Models. *Chemistry of Materials* **26**, 3716-3720 (2014).

15. Pryde AKA, Hammonds KD, Dove MT, Heine V, Gale JD, Warren MC. Origin of the negative thermal expansion in and. *J Phys-Condens Matter* **8**, 10973-10982 (1996).
16. Pryde AK, Hammonds KD, Dove MT, Heine V, Gale JD, Warren MC. Rigid unit modes and the negative thermal expansion in ZrW_2O_8 . *Phase Transitions* **61**, 141-153 (1997).
17. Tucker MG, Goodwin AL, Dove MT, Keen DA, Wells SA, Evans JSO. Negative Thermal Expansion in ZrW_2O_8 : Mechanisms, Rigid Unit Modes, and Neutron Total Scattering. *Phys Rev Lett* **95**, 255501 (2005).
18. Ravindran TR, Arora AK, Mary TA. High Pressure Behavior of ZrW_2O_8 : Gruneisen Parameter and Thermal Properties. *Phys Rev Lett* **84**, 3879-3882 (2000).
19. Evans JSO, Hu Z, Jorgensen JD, Argyriou DN, Short S, Sleight AW. Compressibility, Phase Transitions, and Oxygen Migration in Zirconium Tungstate, ZrW_2O_8 . *Science* **275**, 61-65 (1997).
20. Speedy RJ. Models for the amorphization of compressed crystals. *J Phys-Condens Matter* **8**, 10907-10918 (1996).
21. Varga T, Wilkinson AP, Jupe AC, Lind C, Bassett WA, Zha C-S. Pressure-induced amorphization of cubic ZrW_2O_8 studied in situ and ex situ by synchrotron x-ray diffraction and absorption. *Phys Rev B* **72**, 024117 (2005).
22. Arora AK, Sastry VS, Sahu PC, Mary TA. The pressure-amorphized state in zirconium tungstate: a precursor to decomposition. *J Phys-Condens Matter* **16**, 1025-1031 (2004).
23. Keen DA, *et al.* Structural Description of Pressure-Induced Amorphization in ZrW_2O_8 . *Phys Rev Lett* **98**, 225501 (2007).
24. Figueirêdo CA, *et al.* Compression mechanism and pressure-induced amorphization of ZrW_2O_8 . *Phys Rev B* **76**, 184201 (2007).
25. Pantea C, *et al.* Pressure-induced elastic softening of monocrystalline zirconium tungstate at 300 K. *Phys Rev B* **73**, 214118 (2006).
26. Zhang L, Han J, Wang H, Car R, Weinan E. Deep potential molecular dynamics: a scalable model with the accuracy of quantum mechanics. *Phys Rev Lett* **120**, 143001 (2018).
27. Zhang L, Han J, Wang H, Saidi WA, Car R. End-to-end symmetry preserving inter-atomic potential energy model for finite and extended systems, in Proceedings of the 32nd International Conference on Neural Information Processing Systems, NIPS'18 (Curran Associates, Inc., Red Hook, NY, 2018), pp. 4441–4451.

28. Wen T, Zhang L, Wang H, E W, Srolovitz DJ. Deep potentials for materials science. *Materials Futures* **1**, 022601 (2022).
29. Deringer VL, *et al.* Origins of structural and electronic transitions in disordered silicon. *Nature* **589**, 59-64 (2021).
30. Zhang L, Wang H, Car R, E W. Phase Diagram of a Deep Potential Water Model. *Phys Rev Lett* **126**, 236001 (2021).
31. He R, *et al.* Structural phase transitions in SrTiO₃ from deep potential molecular dynamics. *Phys Rev B* **105**, 064104 (2022).
32. Niu H, Bonati L, Piaggi PM, Parrinello M. Ab initio phase diagram and nucleation of gallium. *Nat Commun* **11**, 2654 (2020).
33. Calegari Andrade MF, Ko H-Y, Zhang L, Car R, Selloni A. Free energy of proton transfer at the water-TiO₂ interface from ab initio deep potential molecular dynamics. *Chemical Science* **11**, 2335-2341 (2020).
34. Zeng J, Cao L, Xu M, Zhu T, Zhang JZH. Complex reaction processes in combustion unraveled by neural network-based molecular dynamics simulation. *Nat Commun* **11**, 5713 (2020).
35. Nakata H, Filatov M, Choi CH. Accelerated Deep Learning Dynamics for Atomic Layer Deposition of Al(Me)₃ and Water on OH/Si(111). *ACS Appl Mater Interfaces* **14**, 26116-26127 (2022).
36. Zhang Y, *et al.* DP-GEN: A concurrent learning platform for the generation of reliable deep learning based potential energy models. *Computer Physics Communications* **253**, 107206 (2020).
37. Greathouse JA, Weck PF, Gordon ME, Kim E, Bryan CR. Molecular dynamics simulation of zirconium tungstate amorphization and the amorphous-crystalline interface. *J Phys-Condens Matter* **32**, 085401 (2019).
38. Li J, Meng S, Qin L, Lu H. First-principles study of electronic structure, optical and phonon properties of α -ZrW₂O₈. *Solid State Communications* **247**, 58-63 (2016).
39. Duan N, Kameswari U, Sleight AW. Further Contraction of ZrW₂O₈. *Journal of the American Chemical Society* **121**, 10432-10433 (1999).
40. Catafesta J, Zorzi JE, Perottoni CA, Gallas MR, Da Jornada JAH. Tunable Linear Thermal Expansion Coefficient of Amorphous Zirconium Tungstate. *Journal of the American Ceramic Society* **89**, 2341-2344 (2006).

41. Wang H, Zhang L, Han J, E W. DeePMD-kit: A deep learning package for many-body potential energy representation and molecular dynamics. *Computer Physics Communications* **228**, 178-184 (2018).
42. Lu D, *et al.* DP Train, then DP Compress: Model Compression in Deep Potential Molecular Dynamics. Preprint at <https://ui.adsabs.harvard.edu/abs/2021arXiv210702103L> (2021).
43. Kresse G, Furthmüller J. Efficient iterative schemes for ab initio total-energy calculations using a plane-wave basis set. *Phys Rev B* **54**, 11169-11186 (1996).
44. Kresse G, Furthmüller J. Efficiency of ab-initio total energy calculations for metals and semiconductors using a plane-wave basis set. *Comput Mater Sci* **6**, 15-50 (1996).
45. Perdew JP, Burke K, Ernzerhof M. Generalized Gradient Approximation Made Simple. *Phys Rev Lett* **78**, 1396-1396 (1997).
46. Plimpton S. Fast Parallel Algorithms for Short-Range Molecular Dynamics. *Journal of Computational Physics* **117**, 1-19 (1995).
47. Nosé S. A unified formulation of the constant temperature molecular dynamics methods. *The Journal of Chemical Physics* **81**, 511-519 (1984).
48. Parrinello, M. & Rahman, A. Polymorphic transitions in single crystals: a new molecular dynamics method. *J. Appl. Phys.* **52**, 7182–7190 (1981).
49. <https://dplibrary.deepmd.net/>